Tapish Agarwal
Turbomachinery and Heat Transfer Laboratory,
Department of Aeronautical Engineering,
Technion–Israel Institute of Technology Technion City,
Haifa 32000, Israel
e-mail: tapish@campus.technion.ac.il

Maximilian Stratmann
Turbomachinery and Heat Transfer Laboratory,
Department of Aeronautical Engineering,
Technion–Israel Institute of Technology Technion City,
Haifa 32000, Israel
e-mail: stratmann.max@campus.technion.ac.il

Simon Julius
Turbomachinery and Heat Transfer Laboratory,
Department of Aeronautical Engineering,
Technion–Israel Institute of Technology Technion City,
Haifa 32000, Israel
e-mail: simonjulius@campus.technion.ac.il

Beni Cukurel
Turbomachinery and Heat Transfer Laboratory,
Department of Aeronautical Engineering,
Technion–Israel Institute of Technology Technion City,
Haifa 32000, Israel
e-mail: beni@cukurel.org

Exploring Applicability of Acoustic Heat Transfer Enhancement Across Various Perturbation Elements

The requirements of improved heat transfer performance on turbine surfaces and internal cooling passages drive the research into exploring new methods for efficiency enhancements. The addition of ribbed structures inside the cooling ducts has proven to be most practical, which increases heat transfer from surfaces to fluid flow at the cost of some pressure loss. Many active and passive methods have been proposed for enhancing the heat transfer, where acoustic excitation has been recently shown to be an effective option. Moreover, the existing pressure fluctuations due to rotor–stator interactions can also be utilized as a source of excitation. However, the sensitivity of the phenomenon to various flow and geometric parameters has not been fully characterized. The present study investigates various aspects of convective heat transfer enhancement and turbulent flow modulation caused by acoustic forcing on separating and reattaching flow over isolated rib obstacles. A parametric study is conducted; rib obstacles of various sizes and shapes (including rectangular, squared, triangular, and semi-cylindrical) are installed in a low-speed, fully turbulent wind tunnel, and measurements are taken at different velocities and excitation frequencies. Static pressure and spatially resolved surface temperature measurements are performed to quantify the ramifications of acoustic excitation on the wetted wall. Within the favorable Strouhal number range of 0.1–0.25, an optimum value of 0.16 is observed. It is shown that triangular ribs are more prone to acoustic heat transfer enhancement than rectangular or cylindrical perturbations. A linear correlation between static pressure recovery rate and acoustic heat transfer enhancement is observed, which is invariant to change in size/shape of the rib as well as flow and excitation parameters.
[DOI: 10.1115/1.4049800]

Keywords: heat transfer enhancement, turbine cooling, acoustic flow control

Introduction

Active and passive flow modulation is a topic of current research toward flow topology enhancement and optimization. The energy equation, describing the temperature field, is strongly impacted by the state of the velocity field. As a consequence, manipulation of the flow field can have dramatic ramifications on the heat transfer properties [1].

Gas Turbine Heat Transfer Enhancement. In gas turbine heat transfer applications, passive elements such as turbulators are commonly used to increase the convective heat transfer across a solid–fluid interface. Transition to turbulence, increased mixing, and flow impingement mechanisms have been shown to enhance heat transfer [2]. While passive mechanisms offer simple and effective approaches toward heat transfer enhancement, they often come at a cost in the form of a pressure penalty [2]. Much needed progress in heat transfer efficacy remains a key driver in the gas turbine community.

Active flow control studies in wall-bounded flows using synthetic jets, mechanical actuators, and other methods have shown the dramatic impact that these approaches can have in modifying fluid–structure interaction [3–6]. Among existing active flow control techniques, many are unsuitable or impracticable in the already complex and demanding environment of a turbine stage. "Global" flow control, via acoustic forcing, provides a simple, minimally invasive approach to heat transfer enhancement.

It has been shown that the existing tonal noise production in turbine stages associated with blade-pass interactions (>150 dB) [7] could be harnessed to provide a "free" enhancement via the selection of appropriate turbulator geometries to instigate Strouhal coupling within the serpentine cooling channels [8]. It was also shown that the base frequency and higher harmonics of turbine serpentine channels are minimally affected by the small-scale features, such as cooling holes, and that the acoustic characteristics of a winding serpentine channel, with 180-deg bends and varying aspect ratio, are remarkably similar to that of a straight, simple tube of equal total length. It was also determined that the resonance frequencies of the serpentine cooling channels are of the same order as the blade-pass frequencies. Finally, it was further demonstrated that the conditions studied within the serpentine channels, including the resonance effects, can be represented by appropriate scalings, matching Reynolds number, sound pressure levels, typical blockage ratios (BRs), and the existence of a scaled resonance condition.

Although the potential for global flow control strategies is clear and has been demonstrated in rib-roughened heat exchangers [9], there is much that remains to be understood on the fundamental aspects of the phenomenon. To this end, there is still a particular benefit to working with canonical geometrical configurations.

Rib Turbulator Shear Layer Dynamics. In the incompressible regime, turbulent flow over a square cylinder rib obstacle contains many of the flow features present in classical turbulator designs,

Contributed by the International Gas Turbine Institute (IGTI) of ASME for publication in the Journal of Turbomachinery. Manuscript received September 20, 2020; final manuscript received November 11, 2020; published online February 12, 2021. Assoc. Editor: David G. Bogard.

while minimizing the added complexity of a strongly three-dimensional flow field [10]. The rib presents an abrupt contraction and re-expansion to the oncoming flow, leading to separation and downstream impingement. At Reynolds numbers $Re_H \approx O[10^4]$, the time-averaged flow field exhibits three recirculation zones comprising four time-averaged vortex structures that form around the rib, positioned in front, on top and two contrarotating vortices in the rib near-wake and wake regions [11].

The free shear layer, originating at the upstream edge, is propelled toward the wall by the low back-pressure zone and impels the instability waves to swirl into spanwise-correlated coherent structures [6,12–15]. The evolution of the shear layer is governed by the formation of vortices and large momentum fluctuations, which convect downstream along with the mixing layer [5,16,19]. As they convect downstream, the vortices undergo spatial growth and vortex pairing interactions. These interactions promote momentum entrainment into the low-pressure region of the obstacle near wake as the shear layer curves downward [19–21]. The downward momentum, induced by the back pressure, leads to wall–vortex interaction and vortex breakdown as the mixing layer impinges on the wall. The strong interaction of the mixing layer with the surface promotes high levels of turbulent mixing on the wall, which inhibits and thus delays boundary layer redevelopment [22–24]. The location of the shear layer impingement demarcates the vicinity of local maximum heat transfer although the precise relationship is a function of the flow thermal history and obstacle geometry [25].

The rib-roughened flow topology greatly enhances channel flow heat transfer via the promotion of mixing, increased wetted area, and flow impingement [26,27]. The role of the wake recirculation region, particularly in the near-wake region, shows that there is an accumulation of heat in this region that contributes to higher local mean temperatures than would be observed in an unribbed channel [28]. It has been shown that the detrimental impact of the recirculation zone on the overall heat transfer enhancement can be mitigated through the application of active flow control [26].

Periodic Excitation of Recirculating Wall-Bounded Flows. Control of bounded and free shear layers is done in practice with the inclusion of periodic flow disturbances either locally (synthetic jets, mechanical flaps, plasma actuators) or comprehensively (e.g., acoustic) to the flow [3]. The mechanisms of enhancement are attributed to the amplification and triggering of instability mechanisms, such as Kelvin–Helmholz or a shedding-type instability [29]. The regularized shedding enhances heat transfer by dislodging the hot fluid in the rib wake and replacing it with the cold fluid from the freestream [27].

Local shear layer modulation via active, periodic forcing has been shown to be conducive to altering the reattachment properties of free shear layers in a myriad of ways. In the literature, it is observed that forcing of the local flow entails higher spreading rates with altered velocity profiles due to stimulation and organization of the vortex merging process [30–32]. Local Strouhal numbers corresponding to subharmonic forcing of the shear layer natural instability frequency are conducive to shear layer modulation [17]. Subharmonic forcing enhances spreading rates by precipitating the shedding of multiple wake flow structures simultaneously, thereby breaking down the sequential shedding of vortex pairs and replacing it with a collective bulk migration of unstable flow features [31]. There is evidence that local excitation mechanisms can induce Strouhal peak lock-in behavior, thus regularizing the shedding structures in the spanwise direction and reducing turbulent reattachment length by as much as 30% in a backward-facing step geometry [33].

Siller and Fernholz [6,34,35] excited the flow upstream of a rib by a local flap and zero-net mass flux oscillating jet in the conducive natural shedding frequency range (corresponding to frequencies around 30 Hz). They reported notable alteration of the shear layer with both forcing methods (40% reduction in reattachment length). They further observed that while the time-averaged length of the recirculation region was reduced, the length of the region where instantaneous reverse-flow occurs remained unchanged. A conducive Strouhal number range of $St = 0.05$, $St = 0.08$, and $St = 0.15 - 0.25$ was reported.

In a previous study [26] on acoustic excitation effects on heat transfer, a wind tunnel operating at 10 m/s freestream velocity was fitted with a rib obstacle (5% blockage ratio) secured to an iso-heat flux heated wall coated with thermochromic liquid crystals (TLCs). A sidewall flush-mounted loudspeaker excited the air cavity at a range of frequencies around the acoustic harmonic resonance frequency. Exclusively at acoustic harmonic resonance, a notable enhancement in the forced convection heat transfer characteristics in the reattachment region downstream of the rib fence was observed.

Global excitation of the flow at an acoustic harmonic resonance frequency of the tunnel air cavity demonstrated a reduction of the reattachment region of up to 37% for forcing amplitude of 130 dB. An enhancement is observed in the Strouhal number range of 0.13–0.25. A generated acoustic sound pressure level of 121 dB was found to be necessary to initiate the instability dynamic [26]. As the sound pressure level is further increased, the heat transfer enhancement increases accordingly.

It is also observed that there is no measurable change in the integral pressure loss with acoustic excitation, which is suggestive of the similar periodic shedding dynamic noted by Siller and Fernholz [6]. Furthermore, the effect of acoustic resonance is only observed downstream of separation. The alteration of the shear layer dynamics was found to correspond to a local heat transfer enhancement of 25% across a single rib fence [26].

Motivation. Despite recent progress in understanding the impact of acoustically modulated forced convection heat transfer on rib-roughened flows, there remain a number of significant gaps in the understanding of the phenomenon. Previous works have reported a weak Strouhal number dependence, with limited available data. There have been no studies correlating the shape of perturbation elements to the acoustic enhancement. This gap in data likely results from the necessity of complex experimental setups required for heat transfer measurements under acoustic excitation. Moreover, this problem of acoustically modulated heat transfer is also difficult to study numerically due to very small time scale requirements.

Along these lines, the motivation of this work is to parametrically study the dependency of acoustic enhanced forced convection on various flow (velocity, excitation frequency) and shape parameters (size, aspect ratio, and geometry). Acoustic modulation has been shown [26] to affect both the heat transfer enhancement and the distribution of static pressure while keeping the overall pressure drop unchanged. Another objective of this study is to create a link between heat transfer enhancement and static pressure measurements, which will enable investigating a broader range of configurations by static pressure measurements alone.

Experimental Methods

Facility. A low-speed open-loop wind tunnel facility (Fig. 1) operating in a suction mode was used for measurements of the present study, precise details of which can be found in a previous publication [36]. The facility was designed with the appropriate scalings to mimic the acoustic resonance, fluid, heat transfer, and acoustic forcing conditions that are present within the serpentine turbine cooling channels [8]. It is powered by a centrifugal blower, which is mechanically decoupled from the test section to prevent the propagation of vibrations induced by the motor. Upstream of the blower, a settling chamber with multiple fine mesh layers further dampens out pressure fluctuations. The 1.5-m long test section is connected to the settling chamber through a 1.8-m constant area duct. The inlet of the facility consists of a

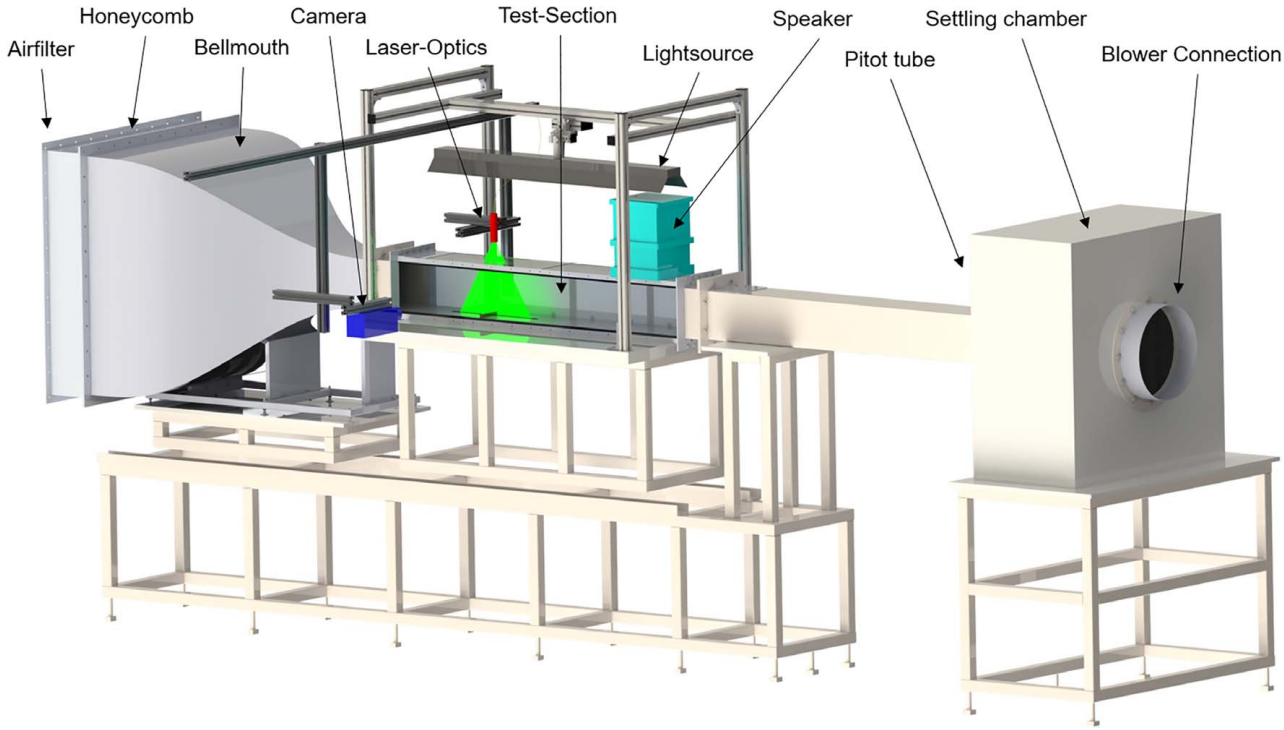

Fig. 1 Wind tunnel facility

honeycomb mounted on a bell mouth inlet with a contraction area ratio of 25 : 1. It is connected to the test section through a 0.12-m long connection piece containing a fine and taut steel wire mesh (25 μm cell size) to introduce a homogeneous turbulence level in the inlet flow [37]. The tunnel has a constant cross-sectional area of 0.2×0.2 m^2 between the exit of the bell mouth and the inlet of the settling chamber. The honeycomb flow straightener with a cell size of 20 mm reduces the swirl and straitens the inflow through reducing the lateral velocity component of the mean flow [37]. The bell mouth is constructed according to Refs. [38,39], such that a high level of flow uniformity is achieved in the working section. The maximum tunnel velocity is 50 m/s.

The tunnel velocity and Reynolds number are calculated from pressure and temperature readings. Static and dynamic pressure is measured upstream of the settling chamber using a Paragon duct mounted air flow measurement station connected to a Scanivalve pressure transducer (Scanivalve Model DSA 3217) with a maximum differential pressure of 2490 Pa (6890 Pa high-pressure side) at an accuracy of ±10 Pa and a Almemo pressure transducer (Ahlborn Almemo Model 2590 DPS) with maximum differential pressure of 10 kPa at an accuracy of ±40 Pa.

Static pressure is measured as differential pressure with respect to the ambient. The ambient temperature is determined via T-type thermocouples, placed upstream of the bell mouth, and inside the settling chamber and acquired with a thermocouple module (24-bit NI TB-9214).

The working section can be fitted with a TLC wall or a plexiglass wall with ports for static pressure measurements and for unsteady microphone measurements.

Acoustic Excitation. Acoustic sound excitation is provided by a loudspeaker (Mackie DLM-8; frequency spectrum of 65 Hz–20 kHz and maximum amplitude of around 140 dB), placed in a sealed casing on top and at the exit of the test section, facing into the working area. A fine and taut steel wire membrane (25 μm cell size) is placed between the channel working section and the speaker cavity, enabling the permeation of acoustic excitation at zero average mass flux into the test section. The maximum speaker sound amplitude is a function of frequency, although typically above 120 dB for all frequencies. Sinusoidal signal input used for the acoustic excitation was provided by a signal conditioner (Tektronic AFG 3021C).

Working Section Measurement Techniques

Static Pressure. Static pressure measurements are conducted using a Scanivalve pressure transducer (Scanivalve Model DSA 3217). The Svanivalve acquires differential pressure in the low-pressure range with an accuracy of ±10 Pa at five ports and in the high-pressure range with an accuracy of ±20 Pa at eight ports.

The wind tunnel test section is fitted with a plexiglass plate containing 57 holes of 2 mm diameter at the centerline. The distance of the ports from the edges is 50 mm, and the spacing between subsequent ports is 15 mm. The region of interest contains 35 measurement locations, which are divided into seven batches of five measurement ports each, connected in turn to the high accuracy Scanivalve ports via a sequence of valves. Static pressure data are acquired at a sampling frequency of 8 Hz across a duration of 120 s and is thus averaged over a total of 960 samples at each port.

The first pressure port is taken as a static reference pressure level from which changes in static pressure across the obstacle ($\Delta p = (p - p_{ref})$) can be deduced. In this study, the static pressure difference has been normalized by the dynamic pressure and further multiplied by the blockage ratio (BR = rib height/channel height). The blockage ratio is found to be a suitable nondimensional parameter with which to normalize for the effect of obstacle height on the pressure drop. It should be noted that there is no impact of any blockage effects on the experimental results.

$$\widetilde{p} = \frac{(p - p_{ref})}{\frac{1}{2}\rho U^2}\frac{1}{\mathrm{BR}} = \frac{\Delta p}{\frac{1}{2}\rho U^2}\frac{1}{\mathrm{BR}} \tag{1}$$

Thermochromic Liquid Crystal. Cholesteric microencapsulated TLCs (R35C20W by Hallcrest Inc.), with an active temperature interval of $35 - 55$°C and a color-play interval within the bandwidth of $\lambda = 400$–700 nm, constitute the final surface coating of a heated

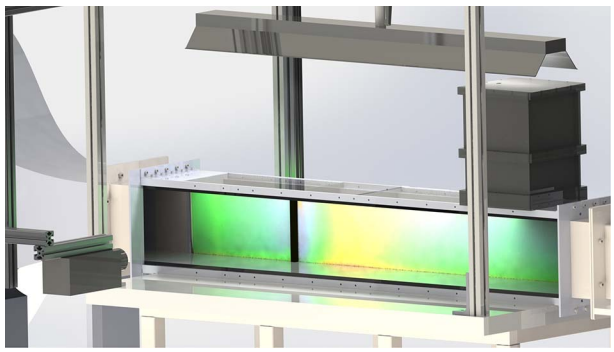

Fig. 2 Setup TLC measurement

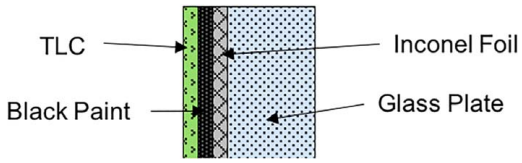

Fig. 3 Cross section TLC plate

sidewall (see Fig. 2). The wall itself is made of tempered glass of thickness $L = 0.01$ m and thermal conductivity $k_g = 0.6$ W/mK, followed by a 25 μm thick Inconel foil-resistive heating element supplied by a DC power supply. This layer is coated with a thin layer of matte black paint to improve the image contrast of the color-play and promote diffuse light reflection. The sidewall is finally coated with the active TLC crystals in solution (see Fig. 3).

The thermoelectric properties of Inconel make it an adequate choice for joule heating as a resistive material providing constant electric resistivity and uniform surface heat flux. At steady state, the majority of the imposed surface heat flux is drawn into the flow. An array of thermocouples positioned behind the plate measure the back plate temperature T_b and allow the heat-flux through the back plate to be accounted for.

$$q = \frac{V \cdot I}{A} - k_g \frac{T_w - T_b}{L} \tag{2}$$

The surface images are acquired by a high-resolution digital camera (Nikon D300S), placed at a 90 deg observation angle from the channel axis. Illumination is provided by a fluorescent light source (OSRAM type T8 L 36 W), mounted 1 m above the test section. To minimize reflections, the test section is surrounded by a black cage, and all surfaces are covered with black cloth.

Thermal equilibrium needs to be reached by operating wind tunnel facility for steady-state data acquisition. Rise times for thermal equilibrium were found experimentally. Temperature measurements for acoustically excited and unexcited flow are recorded subsequently.

High-resolution sRGB images of the active TLC surface are captured in RGB color space, and after background image subtraction, angle correction, and image cropping, the images are transformed into *Hue*-saturation-isntensity color space (HSI) color space using the following equation [26,28,40]:

$$Hue = \frac{1}{2\pi} \cdot \tan^{-1}\left[\sqrt{3} \cdot \frac{G - B}{2R - G - B}\right] \tag{3}$$

This transformation collapses six dimensions into three. A Hue-temperature calibration curve, Fig. 4, is established by an in situ calibration, spanning the entire gamete of color-play (Fig. 5).

The in situ calibration is performed with a special calibration plate (Fig. 5). Seven thermocouples are equally distributed at the

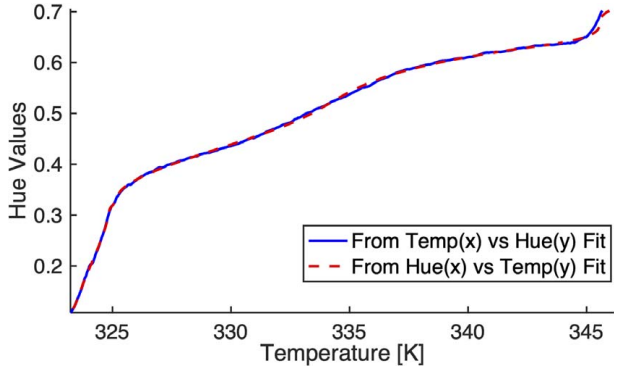

Fig. 4 TLC calibration curve

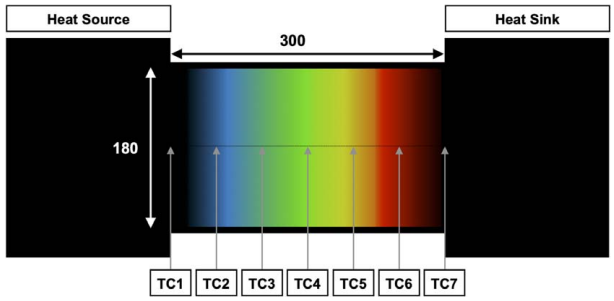

Fig. 5 TLC calibration setup

centerline of the plate, and the left side the plate is heated using a pad heater and the right side cooled by cooling pipes attached to the plate. A 1D steady-state heat conduction condition is achieved in the calibration area, and thermocouple readings and Hue values at the centerline are correlated to their x-position. The x-position is then eliminated by fitting the hue values to temperature values and vice versa. A twice-differentiable, monotonically increasing 20 knots cubic spline provides an exact fit to the calibration data points.

Particle Image Velocimetry. Particle image velocimetry (PIV) measurements for time-averaged recordings were performed using a PIV system consisting of a continuous wave laser (Amtron LS453; 75 W power, 808 nm wavelength) and a high-speed camera (IDT Motion Pro Y7 S1) mounted in the tunnel as shown in Fig. 1. The laser was operated in a continuous mode at maximum power to produce a laser sheet of 2.5 mm thickness and 160 mm width. To avoid reflections, a light-absorbing tape (Acktar Spectral Black) was applied to the rib and the bottom wall surface. A seeding machine (LaVision Aerosol Generator), which produces di-ethyl-hexyl-Sebacat tracer particles with a mean particle diameter of 1 μm, was used to seed the flow. The camera, equipped with a large aperture lens (Nikon NIKKOR 50 mm f/1.2 AI-s), was set to record at 7500 fps, an exposure time of 131 μs at a region of interest of 1920 px width and 688 px height, saving images in 8-bit grayscale. The field of view had a width of 151 mm and a height of 84 mm at a focal plane depth of 2.26 mm. Recordings were processed using the LaVision DaVis 8.4 software package via a cross-correlation algorithm with multi-pass. Velocity vectors were calculated from 7500 recorded frames, correlating each pair of frames (1-2, 2-3, 3-4, 4-5, …) resulting in 7499 vectors. The interrogation windows were of decreasing size from 256 × 256 px, and 50% overlap to 64 × 64 px and 75% overlap. Median filtering was used with a removal peak ratio of <1.2 and interpolation. Vector fields were afterward filtered and smoothed.

Table 1 Static Pressure measurement range

Parameter	Location TE (cm)	Rib Shape	Rib Height (mm)	Rib Width (mm)	f(Hz)	U(m/s)	St	Re_H
Rib size	43.5	Square	10–100	10–100	162	11	0.14–1.5	(6–60) $\times 10^3$
Rib width	43.5	Rectangular	15	5–100	162	11	0.22	9×10^3
Rib height	43.5	Rectangular	10–45	15	162	11	0.14–0.66	$(6-27) \times 10^3$
Location	24–107	Square	15	15	162	11	0.22	9×10^3
U and f	43.5	Square	15	15	100 120 162 200	5–24	0.06–0.6	$(4-20) \times 10^3$
Shape	43.5	Triangles	15	15	162	11	0.22	9×10^3
Shape	43.5	Semi-cylinder	15	30	162	11	0.22	9×10^3

Table 2 TLC measurement range

Parameter	Location TE (cm)	Rib Shape	Rib Height (mm)	Rib Width (mm)	f(Hz)	U(m/s)	St	Re_H
Rib size	43.5	Square	5–100	5–100	162	11	0.07–1.5	$(3–60) \times 10^3$
Rib width	43.5	Rectangular	15	5–100	162	11	0.22	9×10^3
Rib height	43.5	Rectangular	10–30	15	162	11	0.14–0.42	$(6\text{-}18) \times 10^3$
Location	24–85	Square	15	15	162	11	0.22	9×10^3
U and f	43.5	Square	15	15	100 120 162 200	7–24	0.06–0.43	$(6\text{-}20) \times 10^3$

Uncertainty Analysis. The uncertainty in the static pressure measurements is ±0.5% from the manufacturer's specification sheet.

Given the highly complex nature of the TLC measurements, a thorough analysis of the error in the temperature readings must be made. The error associated with distortions in the TLC crystal hue-angle is of the order ±0.25 K. This error is compounded by fluctuations of the order of ±0.2 K in the bulk fluid temperature, the uncertainty of thermocouple reading (±0.35 K), the liquid crystals angular dependency (±0.3 K), and deviation from the hue-temperature curve fit formulation (±0.2 K). This gives an overall wall temperature uncertainty of within ±0.56 K and a relative wall temperature uncertainty of within ±0.3 K.

The relative error in the determination of the heat transfer coefficient and Nusselt number stands at ±1.5%, with the enhancement factor (EF) computing a ±1.5% uncertainty within the 95% confidence bounds. The absolute error is notably more significant due to surface heat flux uncertainty (±2.4%), the back-face conduction loss (up to ±2%), and the Inconel area uncertainty (±1.3%). Along with the uncertainty of convective heat transfer coefficient (±3.5%), hydraulic diameter measurement (±0.56%), and air thermal conductivity (±0.15%), the resulting combined Nusselt number uncertainty is estimated as ±4%.

Results

Flow around perturbation elements depend on a number of flow (velocity, excitation frequency, excitation amplitude, turbulence intensity, etc.) and shape parameters (element size, shape). Tables 1 and 2 present the range of parameters varied for static pressure and TLC measurements, respectively. In addition, Tables 3 and 4 in Appendix B show detailed experimental points for the measurements.

To illustrate the impact of acoustic forcing, the flow field around a rectangular rib is shown in the streamline plot for excited and unexcited flow (Fig. 6). The streamlines are obtained by time-averaging large duration PIV data for both unexcited and excited flow fields. A smaller compressed recirculation bubble with a length of approximately 6H is seen in case of excited flow compared to 10H in case of unexcited flow. The approximate location of reattachment is obtained by considering the location of maximum heat transfer downstream of the rib [25]. Moreover, the streamlines are shifted toward the wall in the excited flow. Let us examine how this reduction in the size of the recirculation zone manifests itself in the static pressure readings.

A sample static pressure measurement over a square rib is presented as a function of distance along the wall in Fig. 7(*a*), for both unexcited and acoustically excited (162 Hz) cases, for a mean flow velocity of 11 m/s corresponding to a Reynolds number Re_H ($= UH/\nu$) of approximately 9×10^3. The boundary layer thickness (δ) immediately upstream of the rib obstacle is estimated to be 3.05 ± 0.15 cm, which results in a boundary layer to the rib height ratio of $\delta/H \approx 2$, and an inlet turbulence intensity of approximately 6 % is measured through PIV. The longitudinal position is normalized by rib height, and the origin is placed below the rib leading edge.

The frequency of excitation is chosen to be 162 Hz as it corresponds to one of the acoustic resonance modes of the tunnel. Since the wind tunnel was designed to scale the acoustic resonances present in turbine serpentine channels, and this frequency also scales to the order of magnitude of typical resonances in the turbine internal cooling passages. The impact of resonance is to establish a standing wave distribution within the tunnel, whereby the acoustic amplitude in the vicinity of a pressure antinode is amplified and reduced in the vicinity of a pressure node.

A typical increase in static pressure before the rib, followed by a sudden drop and then a recovery, is observed. It should be noted that the overall static pressure loss does not change measurably due to excitation. Since the redeveloping flow properties far downstream of the rib are similar, any change in static pressure drop between excited and unexcited cases would also be the same as the total pressure drop. The only difference is that static pressure corresponding to excited flow shows a faster recovery. For quantification of this difference, a pressure recovery enhancement (PRE) over the reattachment length behind the rib is defined.

$$\mathrm{PRE} = \int_{x/H=1}^{x/H=10} (\tilde{p}_{ex} - \tilde{p}_{unex})\, d(x/H) \tag{4}$$

To achieve this, the static pressure values are referenced with respect to their respective downstream minimum values and then normalized by the dynamic pressure and the blockage ratio (Eq. (1)), as shown in Fig. 7(*b*). PRE is defined as the area between excited and unexcited profiles, indicated in gray. The uncertainty in PRE measurements is estimated to be 1%.

The PRE value for the case shown in Fig. 7 is 12.68.

The spatially resolved surface temperature measurements by TLC are used to calculate Nusselt number, Nu ($=qD/k_{air}(T - T_\infty)$), as shown in Fig. 8, over the half plate for unexcited and excited cases. The location of maximum heat transfer on a surface has been shown to in the vicinity of reattachment point [25].

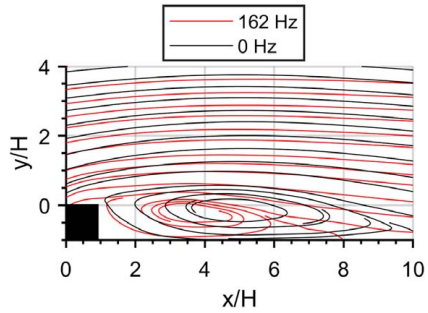

Fig. 6 Time-averaged flow streamlines for excited (162 Hz) and unexcited (0 Hz) flow fields: $H = 1$ cm, $U = 7.5$ m/s, $Re_H = 4.10^3$, and St = 0.22

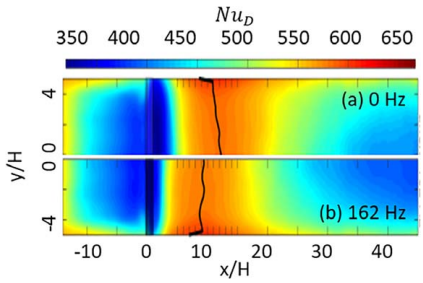

Fig. 8 Spatially resolved Nusselt number values for (*a*) unexcited (0 Hz) and (*b*) excited (162 Hz); half plate is shown; centerline is at $y/H = 0$ for each plot. The black curve corresponds to the location of maximum Nu values. $H = 1.5$ cm, $U = 11$ m/s, $Re_H = 10^4$, and St = 0.22.

Therefore, it can be concluded that excitation results in a smaller reattachment length ($x/H \approx 10$) compared to unexcited case ($x/H \approx 13$).

The centerline values of Nu are shown in Fig. 9(*a*) for excited (162 Hz) and unexcited cases. EF is defined as the ratio between the two Nu profiles (shown in Fig. 9(*b*)).

$$EF = Nu_{ex}/Nu_{unex} \tag{5}$$

An average TEF over the region of reattachment is calculated (Eq. (6)) using the area under the EF curve (gray area in Fig. 9(*b*)).

$$TEF = \frac{100}{9x/H}\int_{x/H=1}^{x/H=10}(EF-1)d(x/H) \tag{6}$$

The average TEF for the case shown in Fig. 9 is 11.26, which translates to an average 11.26% heat transfer enhancement in the region, with an uncertainty of 1.5%.

There are multiple considerations that must be taken into account when determining the appropriate range of integration.

(i) The cause for the enhancement in heat transfer is due to the time-averaged shrinkage of the recirculation region. The region of interest of the TEF plot is where the impact of this mechanism is predominant.

(ii) In a typical heat-exchange application, there are multiple ribs, with a set pitch (spacing) between one another. The spacing is designed to maximize the local enhancement effects. The region of interest in an applied setting is therefore immediately downstream of the rib.

(iii) The temperature field in the tunnel is strongly affected by the flow's "thermal history"; the extent of the heating that the flow has already endured at the point of measurement. With the reduction in the reattachment length in the excited case, the local rate of heat transfer between the flow and the wall is increased. This increase causes a considerable change in the temperature distribution and energy content of the flow. Given that the flow is now "hotter" earlier that it previously was, the rate of enhancement downstream is reduced. This difference can be seen in the discrepancy in TEF far downstream of the rib ($X/H = 35$–40).

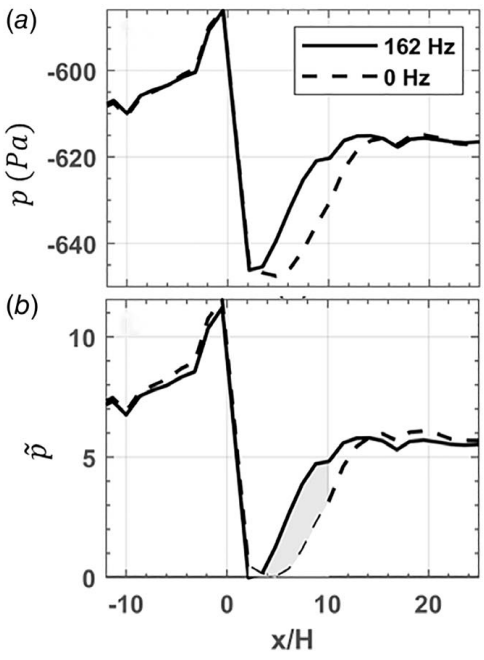

Fig. 7 (*a*) Raw pressure profiles for excited (162 Hz) and unexcited flow and (*b*) referenced and normalized (by dynamic pressure and blockage ratio) pressure profiles; the region of interest for pressure modification by excitation marked in gray; $H = 1.5$ cm, $U = 11$ m/s, $Re_H = 10^4$, St = 0.22

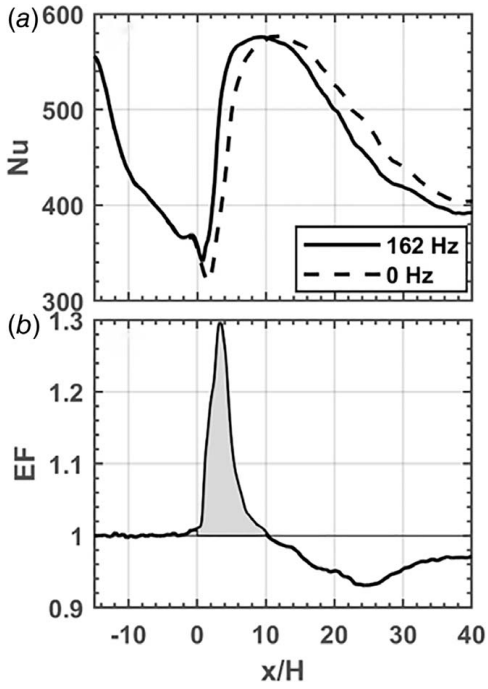

Fig. 9 (*a*) Nu profiles for excited (162 Hz) and unexcited flow and (*b*) EF profile; the region of enhancement used to calculate average thermal enhancement factor (TEF) shown in gray; $H = 1.5$ cm, $U = 11$ m/s, $Re_H = 10^4$, St = 0.22

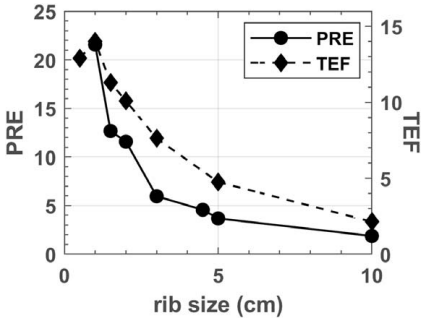

Fig. 10 PRE and TEF profiles for various ribs of square cross sections; $U = 11$ m/s, $f = 162$ Hz

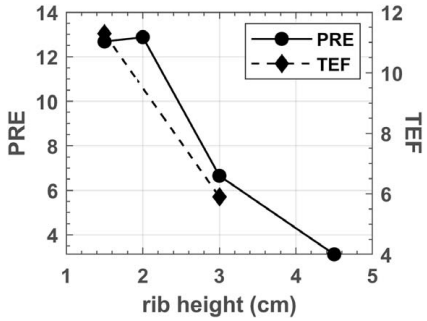

Fig. 12 PRE and TEF profiles for various height of rectangular ribs; $U = 11$ m/s and $f = 162$ Hz

Since it is well understood that the mechanism of enhancement manifests in the shrinkage of the recirculation zone, the approximate location of reattachment of the unexcited flow-field (i.e., 10 H) was selected as an appropriate location to demarcate the end of the span of integration.

One of the objectives of this work is to quantify the effects of change in the shape of perturbation elements on the acoustically enhanced heat transfer phenomenon. For rectangular ribs, the size of square cross section ribs is varied, as well as the height of the ribs while keeping the width constant and vice versa. Figure 10 shows PRE and TEF for various square rib sizes (from 0.5 cm to 10 cm), for a fixed mean flow velocity of 11 m/s and an excitation frequency of 162 Hz resulting in 140 dB of oscillations amplitude. PRE and TEF are seen to correlate closely and indicate a possible optimum rib size of 1 cm, resulting in a 20% heat transfer enhancement.

Similarly, PRE and TEF are plotted (Fig. 11) for variation in the rib width, while keeping the height of the rib constant at 1.5 cm. Mean flow is still maintained by 11 m/s, with 162 Hz excitation. Once again, PRE and TEF correlate closely, and it can be concluded that rectangular ribs of smaller width result in higher pressure recovery enhancement and thermal enhancement under acoustic excitation. This result is reminiscent of the observations of Bearman and Trueman [41] in the case of a rectangular cylinder rigidly suspended in a flow. They found that for high width-to-height ratios, the vortex formation length (which originates at the leading edge) is extended further downstream as a result of the stabilizing influence of the upper surface and the trailing edge corners on the region of vortex formation. Presumably, this stabilizing effect may be further strengthened by the re-establishment of the turbulent boundary layer on the rib top surface, which mitigates the effect of acoustic enhancement.

Keeping the width constant at 1.5 cm and increasing the height also result in a decrease in the two quantification parameters, while both PRE and TEF show similar variation, as shown in Fig. 12.

Owing to the fact that 162 Hz corresponds to one of the acoustic resonance modes of the tunnel, amplitude of fluctuations can be modified by changing the rib location in the tunnel. Microphone measurements are performed at the tunnel wall to estimate the variation of SPL along the length, as shown in Fig. 13(*a*). It shows the presence of a pressure node at around 0.4 m and a pressure antinode at around 1 m. PRE and TEF are shown for the change in location of 1.5 cm square rib, while keeping the flow velocity and excitation frequency constant at 11 m/s and 162 Hz, respectively, in Fig. 13(*b*). Maximum enhancement is observed near 0.4 m and followed by a minimum at 1 m, which are also the locations of pressure node (velocity antinode) and pressure antinode (velocity node), respectively. This indicates that acoustic enhancement in pressure recovery and heat transfer are correlated with the velocity fluctuations amplitude. The higher the velocity fluctuations amplitude, the higher would be the enhancement in heat transfer. This observation was also made by Blevins [42] when studying the effect of sound on vortex shedding from cylinders suspended in a duct. It suggested that the pressure of acoustic wave in itself is not of importance, and the governing factor, as in the use of mechanical actuators, jets, and dielectric-barrier discharge, is the existence of sufficiently large velocity fluctuations. In addition, it is noted that the boundary layer thickness upstream of the rib varies from approximately 1.5 H–2.5 H, but no variation in the enhancement parameters is observed, which can be attributed to this change in boundary layer thickness.

The magnitudes of PRE and TEF for variation in velocity for the same 162 Hz excitation over a 1.5 cm^2 cross section rib are shown in Fig. 14. PRE and TEF once again show a very strong correlation, and both of them show a peak in their respective magnitudes at

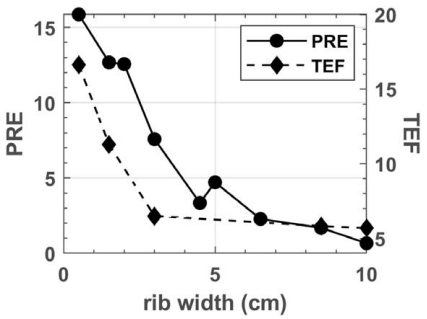

Fig. 11 PRE and TEF profiles for various width of rectangular ribs; $U = 11$ m/s, $f = 162$ Hz, $Re_H = 9 \times 10^3$, and St = 0.22

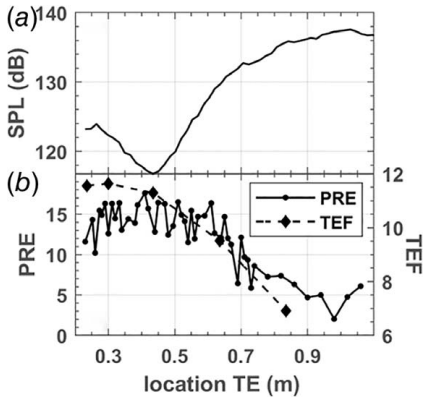

Fig. 13 (*a*) SPL levels as obtained from microphone measurements at the wall inside the tunnel and (*b*) PRE and TEF profiles as a function of rib trailing edge (TE) location in the tunnel; $U = 11$ m/s, $f = 162$ Hz, $H = 1.5$ cm, $Re_H = 9 \times 10^3$, and St = 0.22

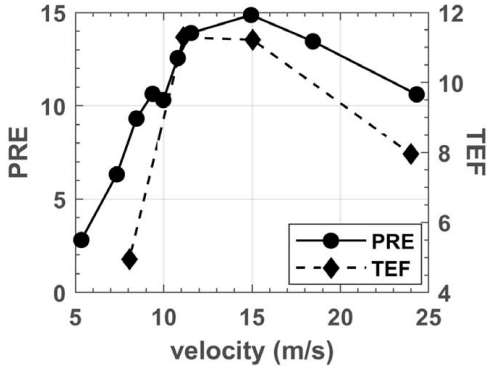

Fig. 14 PRE and TEF profiles for various mean flow velocities; $f = 162$ Hz, $H = 1.5$ cm

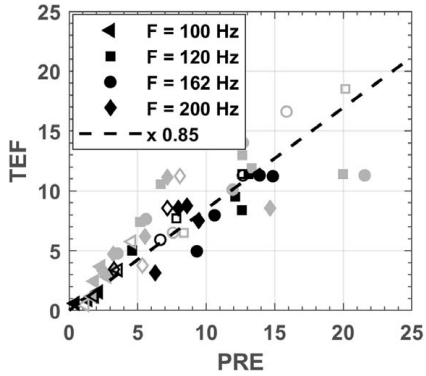

Fig. 16 TEF as a function of PRE for four frequencies of excitation (different symbols) and for different variations of flow parameters (velocity variation (black-filled symbols), square ribs size variation (gray-filled symbols), rib width variation (gray-empty symbols), and rib height variation (black-empty symbols)). The linear fit with TEF = 0.85 × PRE with an r^2 of 0.83.

approximately 15 m/s flow velocity, corresponding to the Strouhal number of 0.162.

This hints at a possible optimum combination of parameters, corresponding to a Strouhal number of 0.162, for maximum enhancement in heat transfer. To explore this further, PRE and TEF as a function of Strouhal number are shown in Fig. 15, for two different frequencies. It is understood that because the Strouhal number takes into account the variation in frequency, one should expect these curves to collapse. But that would be true only if the amplitude of oscillations is the same for all frequencies. Due to experimental limitations, the maximum amplitude that could be reached for 120 Hz and 162 Hz is 136 dB and 140 dB, respectively. The effect of this difference in amplitudes of oscillations can be observed in the respective magnitudes of PRE and TEF for different frequencies. The magnitudes of heat transfer enhancement (TEF) observed for 120 Hz and 162 Hz excitations are 10% and 12%, respectively. Nevertheless, for both frequencies (or amplitudes) of excitations, the optimum Strouhal number value is fixed at approximately 0.16. An additional dip can be observed in the PRE values at St = 0.18 for 120 Hz and St = 0.24 for 162 Hz excitation. This dip is within the uncertainty in the calculations of PRE and therefore should be ignored.

For the considered parametric variations, the magnitudes of PRE and TEF follow similar curves, which implies that there is some correlation between the pressure recovery enhancement and thermal enhancement factors. Figure 16 shows the variation of TEF as a function of PRE for various frequencies of excitation and various changes in flow and rib parameters. It shows a linear correlation, with a slope of 0.86, i.e., doubling PRE results in doubling of TEF. This leads to the conclusion that a quantitative estimate of thermal enhancement can be obtained from only the static pressure measurements, thereby saving the efforts associated with temperature or heat transfer measurements. Even if a different range of integration is used for calculations of PRE and TEF, the relationship between TEF and PRE remains linear as shown in Figs. 18–22 in Appendix B.

In addition to varying the flow parameters and the size of rectangular ribs, the possibility of optimizing the shape of perturbation elements for acoustic enhancement of forced convection heat transfer is also explored. The linear correlation between thermal enhancement and pressure recovery enhancement allowed us to perform only static pressure measurements. The PRE for some of the shapes is shown in Fig. 17 for a flow velocity of 11 m/s and an excitation frequency of 162 Hz. All shapes have a height of 1.5 cm. It is found that compared to the semi-cylinder, the square rib has much higher PRE, which might be because of larger concentrated vortex shedding from the leading edge of the square rib. Taking away the downstream edge of the square rib did not have a significant effect on PRE, as shown with the second and third points in Fig. 17. Changing the orientation of the triangle to an upstream slope leads to a significant increase in the pressure recovery to a PRE value of 22. Using the linear relation obtained in Fig. 16, an enhancement in heat transfer due to acoustic excitation alone is expected to be around 20%.

It should be noted that the Strouhal dependence indicates the existence of shedding events at a characteristic, velocity and geometry-specific, frequency. It has been demonstrated by

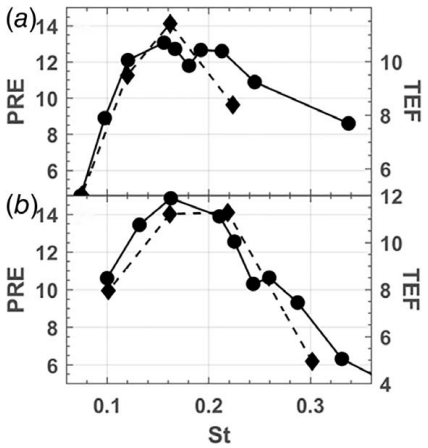

Fig. 15 PRE and TEF profiles as a function of Strouhal number, St, for three frequencies of excitation: (*a*) 120 Hz and (*b*) 162 Hz; $U = 11$ m/s, $Re_H = 9 \times 10^3$

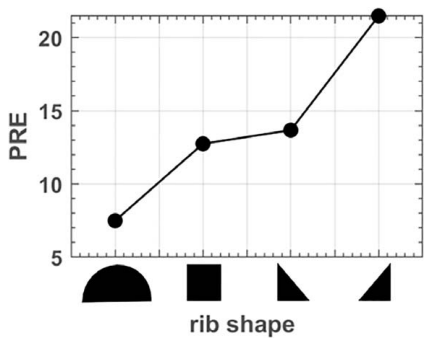

Fig. 17 Variation of PRE for change in shape of perturbation elements: starting from left: semi cylinder, square, isosceles right angle triangle with downstream slope, and with upstream slope $U = 11$ m/s, $f = 162$ Hz, $H = 1.5$ cm, $Re_H = 9 \times 10^3$, St = 0.22

Ref. [43] that the characteristic shedding frequency is associated with the separation distance between the shear layers (wall and free shear layer in this case), as well as the base pressure [43,44]. This being the case, the enhancement effect is not strictly related to the bluff-body geometry itself, but rather, is determined by the relationship between the distance and the shear layers, which is approximately the obstacle height and the velocity field. These experiments indicate that differences in geometry can impact the base pressure, primarily by affecting the velocity profile around the obstacle. The acoustic enhancement effect is therefore expected for all geometrical topologies, as it is driven by the Strouhal coupling phenomenon—a function of obstacle height and back pressure.

Conclusion

Heat transfer enhancement by acoustic excitation remains an attractive topic of research due to the possibility of providing heat transfer enhancement with negligible added pressure penalties. This is particularly the case in gas turbines, where the acoustic source is very loud [7] and results from the turbine–stage blade–pass interactions. The previous work has demonstrated the potential applicability of this to improve the heat transfer within the turbine blade serpentine cooling channels [8].

This parametric study, performed at the appropriate scalings to mimic the physics within these serpentine passages, encompasses various physical, flow, and excitation parameters affecting the acoustically excited heat transfer, through wall static pressure and surface heat transfer measurements. It is demonstrated that there is a conducive peak in the Strouhal number at around St values of 0.16. It was further noted that the effect of acoustic forcing is diminished by increasing rib width, which is possibly due to the stabilizing effect of the rib topside on the vortex formation length. The linear correlation between the integrated pressure recovery enhancement and thermal enhancement factor paves the way for simpler cold flow experiments towards future investigations of acoustically excited heat transfer enhancement. Furthermore, it was confirmed that velocity fluctuation amplitudes and not the pressure fluctuation amplitudes are correlated to the heat transfer enhancements. The importance of rib geometry in acoustic heat transfer enhancement is shown by changing shape from a semi-cylinder to an upstream slope right-angled triangle, resulting in three fold increase receptivity to acoustic excitation.

Lessons Learned

For acoustic enhancement of forced convection heat transfer over perturbation elements.

(1) Optimum Strouhal number is approximately 0.16.
(2) Receptivity of triangular ribs is greater than square ribs, which is higher than semi-cylindrical ribs.
(3) There is a direct correlation with amplitude of velocity oscillations not necessarily the local sound pressure level.
(4) There is a direct correlation of thermal enhancement to pressure recovery rate.

Acknowledgment

The present research work was partially supported by Israel Science Foundation under grant 1752/15. The authors also acknowledge the financial support by Minerva foundation via contract AZ5746940764.

Conflict of Interest

There are no conflicts of interest.

Data Availability Statement

The datasets generated and supporting the findings of this article are obtainable from the corresponding author upon reasonable request. The authors attest that all data for this study are included in the paper.

Nomenclature

Symbols

f = sound excitation frequency (Hz)
k = thermal conductivity (W/m*K)
p = pressure (Pa)
q = heat flux per unit area (W/m^2)
x = freestream direction (m)
y = transverse direction (m)
z = spanwise direction (m)
A = Joule heated area (m^2)
B = intensity of blue in RGB color space (–)
D = hydraulic diameter of test section (m)
F = acquisition frequency (Hz)
G = intensity of green in RGB color space (–)
H = rib height (m)
I = eccentric current (A)
L = thickness of glass plate (m)
R = intensity of red in RGB color space (–)
T = temperature (K)
U = mean flow velocity (m/s)
V = voltage (V)
$\tilde{p}$ = normalized pressure (–)
Re_H = Reynolds number based on rib height (–)
r^2 = statistical coefficient of determination (–)
fps = frames per second (1/s)
px = number of Pixel (–)
BR = blockage ratio (–)
EF = enhancement factor (–)
Nu = Nusselt number (–)
PRE = pressure recovery enhancement (–)
Re = Reynolds number (–)
St = Strouhal number (–)
SPL = sound pressure level (dB)
TEF = thermal enhancement factor (–)
TL = rib obstacle trailing edge location (m)
Hue = angle of HSI color space (rad)
$\triangle$ = difference operator (–)
λ = light wavelength (nm)
ρ = density (kg/m^3)

Subscripts

$acqu$ = acquisition
air = air
b = back of the plate
dyn = dynamic
ex = excited
g = glass
opt = optimal
ref = reference
$unex$ = unexcited
w = wall
∞ = freestream

Appendix A: Dependence of Thermal Enhancement Factor and Pressure Recovery Enhancement Ratio on the Range of Integration

Figures 18–22 show the TEF as a function PRE for various range of integrations.

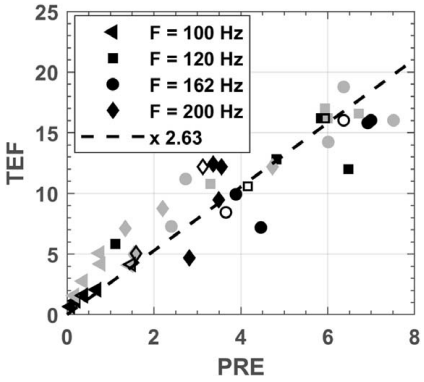

Fig. 18 TEF as a function of PRE for four frequencies of excitation (different symbols) and for different variations of flow parameters (velocity variation (black-filled symbols), square ribs size variation (gray-filled symbols), and rib height variation (black-empty symbols)), and the linear fit with TEF = 2.63 × PRE; for integration over 7 rib heights downstream of the rib

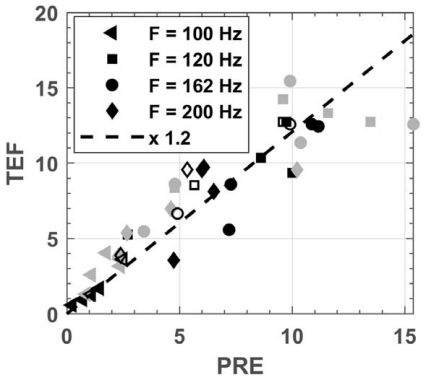

Fig. 19 TEF as a function of PRE for four frequencies of excitation (different symbols) and for different variations of flow parameters (velocity variation (black-filled symbols), square ribs size variation (gray-filled symbols), and rib height variation (black-empty symbols)), and the linear fit with TEF = 1.2 × PRE; for integration over 9 rib heights downstream of the rib

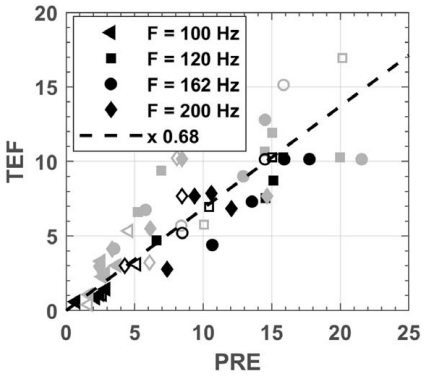

Fig. 20 TEF as a function of PRE for four frequencies of excitation (different symbols) and for different variations of flow parameters (velocity variation (black-filled symbols), square ribs size variation (gray-filled symbols), rib width variation (gray-empty symbols), and rib height variation (black-empty symbols)), and the linear fit with TEF = 0.68 × PRE; for integration over 11 rib heights downstream of the rib

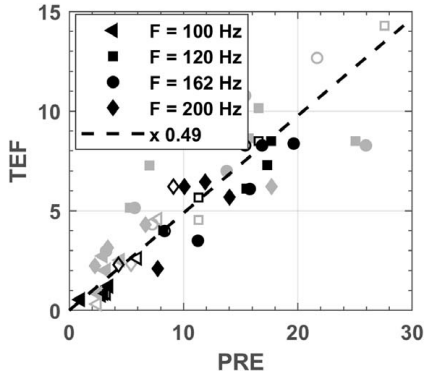

Fig. 21 TEF as a function of PRE for four frequencies of excitation (different symbols) and for different variations of flow parameters (velocity variation (black-filled symbols), square ribs size variation (gray-filled symbols), rib width variation (gray-empty symbols), and rib height variation (black-empty symbols)), and the linear fit with TEF = 0.49 × PRE; for integration over 13 rib heights downstream of the rib

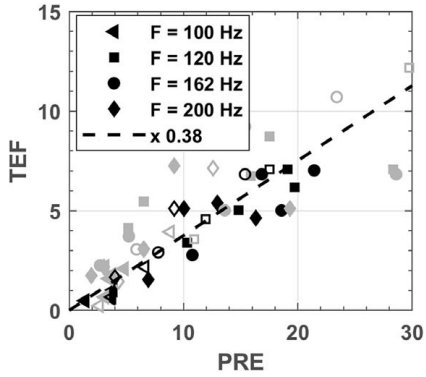

Fig. 22 TEF as a function of PRE for four frequencies of excitation (different symbols) and for different variations of flow parameters (velocity variation (black-filled symbols), square ribs size variation (gray-filled symbols), rib width variation (gray-empty symbols), and rib height variation (black-empty symbols)), and the linear fit with TEF = 0.38 × PRE; for integration over 15 rib heights downstream of the rib

Appendix B: Experimental Points

Table 3 Combination of physical parameters for static pressure measurements

Rib size variation							
Width, height (mm)	10	15	20	30	45	50	100
St	0.15	0.22	0.29	0.44	0.66	0.74	1.47
Re_H	6×10^3	9×10^3	1×10^4	2×10^4	3×10^4	3×10^4	6×10^4
U = 11 m/s, f = 162 Hz, Rib shape = Square, TE location = 43.5 cm							
Rib width variation							
Width (mm)	5	15	20	30	45	50	65	85	100
Height = 15 mm, U = 11 m/s, f = 162 Hz, Rib shape = Rectangular, TE location = 43.5 cm, $Re_H = 9\times10^3$, St = 0.22									
Rib height variation							
Height (mm)	15	20	30	45			
St	0.22	0.29	0.44	0.66			
Re_H	9×10^3	1×10^4	2×10^4	3×10^4			
Rib width = 15 mm, U = 11 m/s, f = 162 Hz, Rib shape = Rectangular, TE location = 43.5 cm							
Location variation							
Location TE = 23.5 – 107 cm (50 locations)							
Width = Height = 15 mm, U = 11 m/s, f = 162 Hz, Rib shape = Square, $Re_H = 9\times10^3$, St = 0.22							
Rib velocity variation							
Velocity (m/s)	5.3	7.3	8.5	9.4	10.0	10.8	11.5	14.9	18.4	24.3
Re_H	4×10^3	6×10^3	7×10^3	8×10^3	8×10^3	9×10^3	1×10^4	1×10^4	2×10^4	2×10^4
f = 120 Hz										
St	0.34	0.25	0.21	0.19	0.18	0.17	0.16	0.12	0.10	0.07
f = 162 Hz										
St	0.46	0.33	0.29	0.26	0.24	0.23	0.21	0.16	0.13	0.10
Width = Height = 15 mm, Rib shape = square, TE location = 43.5 cm										

Rib shape variation		
	Height (mm)	Width (mm)
Shape 1: Semi-cylinder	15	30
Shape 2: Downstream slope right-angled isosceles triangle	15	15
Shape 3: Upstream slope right-angled isosceles triangle	15	15
U = 11 m/s, f = 162 Hz, $Re_H = 9\times10^3$ TE location = 43.5 cm		

Table 4 Combination of physical parameters for TLC measurements

Rib size variation							
Width, height (mm)	5	10	15	20	30	50	100
St	0.07	0.15	0.22	0.29	0.44	0.74	1.47
Re_H	3×10^3	6×10^3	9×10^3	1×10^4	2×10^4	3×10^4	6×10^4
U = 11 m/s, f = 162 Hz, Rib shape = Square, TE location = 43.5 cm							
Rib width variation							
Width (mm)	5	15	30	100			
Height = 15 mm, U = 11 m/s, f = 162 Hz, Rib shape = Rectangular, TE location = 43.5 cm, $Re_H = 9\times10^3$, St = 0.22							
Rib height variation							
Height (mm)	15	20					
St	0.22	0.29					
Re_H	9×10^3	1×10^4					
Rib width = 15 mm, U = 11 m/s, f = 162 Hz, Rib shape = Rectangular, TE location = 43.5 cm							
Rib location variation							
Location TE (cm)	23.5	30	43.5	63.5	83.5		
Width = Height = 15 mm, U = 11 m/s, f = 162 Hz, Rib shape = Square, $Re_H = 9\times10^3$, St = 0.22							
Rib velocity variation							
Velocity (m/s)	8	11	15	24			
Re_H	7×10^3	9×10^3	1×10^4	2×10^4			
f = 100 Hz, St	0.19	0.14	0.10	0.06			
f = 120 Hz, St	0.23	0.16	0.12	0.08			
f = 162 Hz, St	0.30	0.22	0.16	0.10			
f = 200 Hz, St	0.38	0.27	0.20	0.16			
Width = Height = 15 mm, Rib shape = Square, TE location = 43.5 cm							

References

[1] Schlichting, H., and Gersten, K., 2017, *Boundary-Layer Theory*, 9th ed., Springer-Verlag Berlin Heidelberg, New York.
[2] Ligrani, P. M., Oliveira, M. M., and Blaskovich, T., 2003, "Comparison of Heat Transfer Augmentation Techniques," AIAA J., **41**(3), pp. 337–362.
[3] Rice, E., and Zaman, K., 1987, "Control of Shear Flows by Artificial Excitation," 11th Aeroacoustics Conference, Sunnyvale, CA, Oct. 19–21 .
[4] Greenblatt, D., and Wygnanski, I. J., 2000, "Control of Flow Separation by Periodic Excitation," Progress Aeros. Sci., **36**(7), pp. 487–545.
[5] Ho, C., and Huerre, P., 1984, "Perturbed Free Shear Layers," Ann. Rev. Fluid Mech., **16**(1), pp. 365–422.
[6] Siller, H. A., and Fernholz, H. H., 2007, "Manipulation of the Reverse-flow Region Downstream of a Fence by Spanwise Vortices," Eur. J. Mech., B/Fluids, **26**(2), pp. 236–257.
[7] Dykas, S., and Machalica, D., 2014, "The Analysis of the Noise Generation in Gas Turbine Stage," Open J. Acoust., **4**(4), pp. 155–162.
[8] Selcan, C., Cukurel, B., and Shashank, J., 2016, "Heat Transfer Implications of Acoustic Resonances in Turbine Internal Cooling Channels," ASME J. Heat. Transfer., **138**(5), p. 051902.
[9] Gendebien, S., Kleiman, A., Leizeronok, B., and Cukurel, B., 2019, "Experimental Investigation of Forced Convection Enhancement by Acoustic Resonance Excitations in Turbulated Heat Exchangers," ASME J. Turbomach., **142**(2), p. 021005.
[10] Hancock, P. E., 1999, "Measurements of Mean and Fluctuating Wall Shear Stress Beneath Spanwise-Invariant Separation Bubbles," Exp. Fluids, **27**(1), pp. 53–59.
[11] Casarsa, L., and Arts, T., 2005, "Experimental Investigation of the Aerothermal Performance of a High Blockage Rib-Roughened Cooling Channel," ASME J. Turbomach., **127**(3), pp. 580–588.
[12] Simpson, R. L., 1987, "Two-Dimensional Turbulent Separated Flow," AIAA J., **25**(6), pp. 775–776.
[13] Siller, H. A., and Fernholz, H. H., 2001, "Separation Behaviour in Front of a Two-Dimensional Fence," Eur. J. Mech., B/Fluids, **20**(5), pp. 727–740.
[14] Bradshaw, P., and Wong, F. Y. F., 1972, "The Reattachment and Relaxation of a Turbulent Shear Layer," J. Fluid. Mech., **52**(1), pp. 113–135.
[15] Fernholz, H. H., 1994, *Fluid- and Gas Dynamics*, Vol. 4, B. K. Schnerr, G.H. Bohning, and W. Frank, eds., Springer, Vienna, pp. 57–67.
[16] Browand, F. K., and Troutt, T. R., 1980, "A Note on Spanwise Structure in the Two-Dimensional Mixing Layer," J. Fluid. Mech., **97**(4), pp. 771–781.
[17] Ho, C. M., and Huang, L. S., 1982, "Subharmonics and Vortex Merging in Mixing Layers," J. Fluid. Mech., **119**(1), pp. 443–473.
[18] Brown, G. L., and Roshko, A., 1974, "On Density Effects and Large Structure in Turbulent Mixing Layers," J. Fluid. Mech., **64**(4), pp. 775–816.
[19] Winant, C. D., and Browand, F. K., 1974, "Vortex Pairing : The Mechanism of Turbulent Mixing-Layer Growth at Moderate Reynolds Number," J. Fluid. Mech., **63**(2), pp. 237–255.
[20] Browand, F. K., and Troutt, T. R., 1985, "The Turbulent Mixing Layer: Geometry of Large Vortices," J. Fluid. Mech., **158**, pp. 489–509.
[21] Troutt, T. R., Scheelke, B., and Norman, T. R., 1984, "Organized Structures in a Reattaching Separated Flow Field," J. Fluid. Mech., **143**, pp. 413–427.
[22] Eaton, J. K., and Johnston, J. P., 1981, "A Review of Research on Subsonic Turbulent-Flow Reattachment," AIAA , **19**(9), pp. 1093–1100.
[23] Chandrsuda, C., and Bradshaw, P., 1981, "Turbulence Structure of a Reattaching Mixing Layer," J. Fluid. Mech., **110**, pp. 171–194.
[24] Kim, J., Kline, S. J., and Johnston, J. P., 1980, "Investigation of a Reattaching Turbulent Shear Layer: Flow Over a Backward-Facing Step," J. Fluid. Eng., **102**(3), p. 302.
[25] Sparrow, E. M., Kang, S. S., and Chuck, W., 1987, "Relation Between the Points of Flow Reattachment and Maximum Heat Transfer for Regions of Flow Separation," Int. J. Heat. Mass. Transfer., **30**(7), pp. 1237–1246.
[26] Cukurel, B., Selcan, C., and Stratmann, M., 2015, "Convective Heat Transfer Investigation of Acoustically Excited Flow Over an Isolated Rib Obstacle," Int. J. Heat Mass Transfer, **91**, pp. 848–860.
[27] Gu, H., Yao, M., Zhao, P., Li, X., and Liu, M., 2018, "Numerical Simulation of Manipulated Flow and Heat Transfer Over Surface-Mounted Rib," Int. J. Therm. Sci., **129**(2016), pp. 124–134.
[28] Cukurel, B., Selcan, C., and Arts, T., 2012, "Color Theory Perception of Steady Wide Band Liquid Crystal Thermometry," Exp. Therm. Fluid. Sci., **39**, pp. 112–122.
[29] Sigurdson, L. W., and Roshko, A., 1988, *Turbulence Management and Relaminarisation*, Vol. 298, Springer, Berlin Heidelberg, pp. 497–514.
[30] Bhattacherjee, S., Scheelke, B., and Troutt, T. R., 1986, "Modification of Vortex Interactions in a Reattaching Separated Flow," AIAA J., **24**(4), pp. 623–629.
[31] Oster, D., and Wygnanski, I., 1982, "The Forced Mixing Layer Betwen Parallel Streams," J. Fluid. Mech., **123**, pp. 91–130.
[32] Browand, F. K., and Latigo, B. O., 1979, "Growth of the Two-Dimensional Mixing Layer From a Turbulent and Nonturbulent Boundary Layer," Phys. Fluids., **22**(6), pp. 1011–1019.
[33] Roos, F. W., and Kegelman, J. T., 1986, "Control of Coherent Structures in Reattaching Laminar and Turbulent Shear Layers," AIAA J., **24**(12), pp. 1956–1963.
[34] Siller, H. A., and Fernholz, H. H., 1996, "Control of the Separated Flow Downstream of a Two-Dimensional Fence by Low-Frequency Forcing," Appl. Sci. Res., **57**(3–4), pp. 309–318.
[35] Siller, H. A., and Fernholz, H. H., 1996, "Turbulent Separation Regions in Front and Downstream of a Fence," *Fluid Mechanics and Its Applications*, Gavrilakis, P.A., Machiels, S., and Monkewitz, L., eds. 36th ed., Springer, Dordrecht, Netherlands, pp. 487–490, Ch. Advances i.
[36] Selcan, C., Cukurel, B., and Shashank, J., 2016, "Experimental Facility Development Toward Sound-Excitation Effects on Forced Convection Heat Transfer," J. Thermophys. Heat. Transfer., **30**(2), pp. 308–317.
[37] Scheiman, J., and Brooks, J. D., 1981, "Comparison of Experimental and Theoretical Turbulence Reduction Characteristics for Screens, Honeycomb, and Honeycomb-Screen Combinations," J. Aircraft, **18**(8), pp. 638–643.
[38] Bell, J. H., and Mehta, R. D., 1989, "Boundary-Layer Predictions for Small Low-Speed Contractions," AIAA J., **27**(3), pp. 372–374.
[39] Bethea, R. M., and Rhinehart, R. R., 1991, *Applied Engineering Statistics*, Marcel Dekker Inc., New York.
[40] Farina, D. J., Hacker, J. M., Moffat, R. J., and Eaton, J. K., 1994, "Illuminant Invariant Calibration of Thermochromic Liquid Crystals," Exp. Therm. Fluid. Sci., **9**(1), pp. 1–12.
[41] Bearman, P. W., and Trueman, D. M., 1972, "An Investigation of the Flow Around Rectangular Cylinders," Aeronautical Q., **23**(3), pp. 229–237.
[42] Blevins, R. D., 1985, "The Effect of Sound on Vortex Shedding From Cylinders," J. Fluid. Mech., **161**, pp. 217–237.
[43] Griffin, O., 1981, "Universal Similarity in the Wakes of Stationary and Vibrating Bluff Structures," ASME. J. Fluids Eng., **103**(1), pp. 52–58.
[44] Griffin, O. M., and Hall, M. S., 1991, "Review-vortex Shedding Lock-on and Flow Control in Bluff Body Wakes," J. Fluids Eng., Trans. ASME, **113**(4), pp. 526–537.